Imaging Torfajökull's Magmatic Plumbing System With Seismic Interferometry and Phase Velocity Surface Wave Tomography

Martins, Joana E.; Ruigrok, Elmer; Draganov, Deyan; Hooper, A.; Hanssen, Ramon; White, R.S.; Soosalu, Heidi

DOI
10.1029/2018JB016002

Publication date
2019

Document Version
Final published version

Published in
Journal of Geophysical Research: Solid Earth

JGR Solid Earth

RESEARCH ARTICLE
10.1029/2018JB016002

Imaging Torfajökull's Magmatic Plumbing System With Seismic Interferometry and Phase Velocity Surface Wave Tomography

J. E. Martins[1,2], E. Ruigrok[3,4], D. Draganov[1], A. Hooper[5], R. F. Hanssen[1], R. S. White[6], and H. Soosalu[6,7]

[1]Department of Geoscience and Remote Sensing, Delft University of Technology, Delft, Netherlands, [2]Advisory Group for Business Affairs, TNO, Utrecht, Netherlands, [3]Department of Earth Sciences, Utrecht University, Utrecht, Netherlands, [4]Royal Netherlands Meteorological, De Bilt, Netherlands, [5]School of Earth and Environment, University of Leeds, Leeds, UK, [6]Department of Earth Sciences, University of Cambridge, Cambridge, UK, [7]Department of Geological Mapping and Geological Data, Geological Survey of Estonia, Tallinn, Estonia

Abstract Torfajökull volcano, Iceland, has not erupted since 1477. However, intense geothermal activity, deformation, and seismicity suggest a long-lasting magmatic system. In this paper, we use ambient noise tomography to image the magmatic system beneath Torfajökull volcano. One hundred days of ambient noise data from 23 broadband seismometers show the consistent presence of double-frequency microseism noise with significant power between ~0.1 and 0.5 Hz. Beamforming results indicate microseism noise with persistent higher energy propagating from west and SE directions and apparent velocities below 3 km/s. We use ambient noise seismic interferometry to retrieve Rayleigh waves, and we introduce a method to estimate the reliability of the retrieved surface waves. We find stable estimation of surface wave phase velocities between 0.16 and 0.38 Hz. Azimuthal velocity variations show a trend of higher velocities in the NE/SW direction, the strike of the rift zone intersecting Torfajökull, and orientation of erupted lavas on a NE-SW fissure swarm. Tomographic results indicate low-velocity anomalies beneath the volcano caldera (between −5% and −10%) and even lower velocity variations in the southeast and southwest study area (below −10%), outside the volcano caldera. Low anomalies may indicate the existence of hot material, more prominent outside the caldera outskirts. High-velocity variations (between 5% and 10%) outline the volcano caldera between 4- and 5-km depth and more pronounced velocities (between 10% and 15%) up to 5-km depth in the north of the volcano caldera. We interpret the former as possible caldera collapse structure and the latest as solidified intrusive magma from the old preferred magma paths.

Plain Language Summary Magmatic plumbing systems' characterization is one of the pillars for predicting volcanic eruptions. While most of the active volcanoes are being currently monitored, less is known about volcanoes that had not erupted recently. Torfajökull volcano, Iceland, has not erupted since 1477. However, intense geothermal activity, deformation, and seismicity suggest a long-lasting magmatic system. We use ambient noise to produce a tomographic image of the magmatic system beneath Torfajökull volcano. This technique allows us to detect velocity variations/contrasts due to changes in composition, density, temperature, or pressure in the subsurface.We identify high-velocity variations outlining the volcano caldera between 4- and 5-km depth and more pronounced high-velocities at shallower depths in the north of the volcano caldera. We interpret the former as possible caldera collapse structure and the latest as solidified (and dense) intrusive magma from the old preferred magma paths. The tomographic results also indicate low-velocity anomalies beneath the volcano caldera and even lower-velocity variations in the southeast and southwest study area, outside the volcano caldera. The most prominent low-velocity features are located outside the volcano caldera outskirts. These low anomalies, or deceleration areas of wave velocity, may indicate the existence of hot material (molten or partially molten rock).

Key Points:
- This article presents the first tomographic image (3-D *S* wave velocities) of Torfajökull's magmatic system; we have derived a 3-D *S* wave velocity field from ambient noise tomography
- We developed a new methodology for phase velocity estimation from retrieved surface waves applied to 100 days of recorded ambient noise
- We interpret the low-/high-velocity anomalies interpreted as molten or partial molten cavities/channels (low) and old dike intrusions/caldera forming (high)

Supporting Information:
- Data Set S1
- Supporting Information S1

Correspondence to:
J. E. Martins,
j.c.estevesmartins@tudelft.nl

Citation:
Martins, J. E., Ruigrok, E., Draganov, D., Hooper, A., Hanssen, R. F., White, R. S., & Soosalu, H. (2019). Imaging Torfajökull's magmatic plumbing system with seismic interferometry and phase velocity surface wave tomography. *Journal of Geophysical Research: Solid Earth*, *124*. https://doi.org/10.1029/2018JB016002

Received 27 APR 2018
Accepted 13 FEB 2019
Accepted article online 19 FEB 2019

1. Introduction

Torfajökull has a unique location among Icelandic volcanoes. The volcano lies at the intersection of the rift zone, the extension of the Mid-Atlantic Ridge over Iceland propagating at ~19.8 mm/year (Sella et al., 2002), and the transform zone that connects to Reykjanes Peninsula/ridge (Figure 1a). Located at a neovolcanic

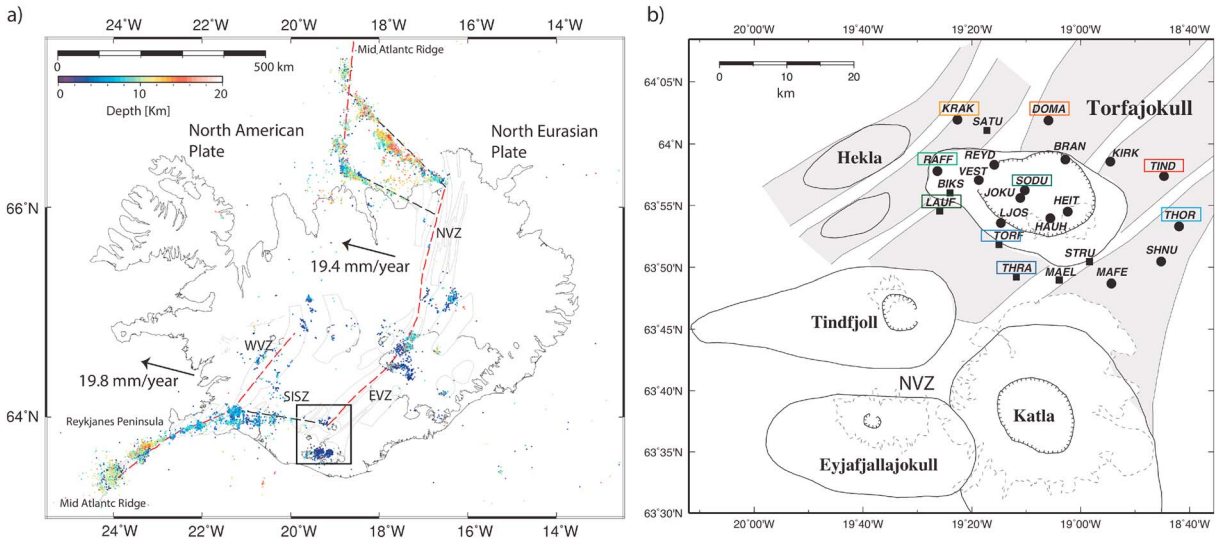

Figure 1. (a) Map of Iceland with tectonic features. The neovolcanic zones, areas with active spreading and plate growth, are identified along with their set of volcanic systems (fissure swarms and central volcano or both) outlined in gray (Einarsson & Saemundsson, 1987). Red dashed lines locate the plate boundary, and black lines locate transform fault systems. Colored dots represent the depths of earthquakes recorded since 1995 delineating the rift and the transform zones (note that depths over the sea areas are not well constrained). In the map are also identified the North Volcanic Zone (NVZ), the Western Volcanic Zone (WVZ), the Eastern Volcanic Zone (EVZ), and the South Iceland Seismic Zone (SISZ). The box in south central of the map locates Torfajökull volcanic system at the intersection of the SISZ and EVZ, immediately north of Katla volcano. The arrows show the full spreading rate of the north American plate (mm/yr) and direction estimated from the REVEL plate motion model (Sella et al., 2002) relative to stable Eurasia. (b) Location of Torfajökull and neighboring volcanoes (square of (a) zoomed in). Black circles and squares locate the seismic network deployed in 2005. Colored squares around station names identify the stations plotted in Figure 2.

area of the Eastern Volcanic Zone (EVZ), Torfajökull has, as direct neighbors, Hekla volcano to the west and Katla volcano to the south, which are among the top three most active Icelandic volcanoes (Figure 1b).

Torfajökull is the largest silicic volcanic center in Iceland with most of its rhyolitic lava flows having erupted subglacially (Tuffen, 2007). Two small ice caps partially cover the southeastern part of the large caldera of about 18 × 12 km. The caldera is cut by fissure swarms stretching to the NE and SW of the central volcano (Soosalu et al., 2006), and it is thought that the caldera collapsed after one or more eruptions, following which it was partially filled in by younger extrusives (Gunnarsson et al., 1998). These younger extrusives involve basaltic magmas mixing events (Blake, 1984; McGarvie, 1984) formed after the tholeiitic basalts are argued to enter into the Torfajökull's silicic center, by lateral propagation, through the fissure swarm of Veidivötn's (Bardarbunga) volcanic system (identified in Figure 1a as EVZ).

Despite Torfajökull's infrequent eruptions, only two in the last 1,200 years, ongoing seismicity, deformation, and geothermal activity within its caldera indicate the continued presence of a still hot magma chamber. Low-frequency earthquakes (1–3 Hz with magnitude <2) argued to be related with active magma movements are detected only at the southeast part of the caldera, extending downward to about 15-km depth (Brandsdóttir & Einarsson, 1992; Soosalu & Einarsson, 2004). The epicentral area of the low-frequency earthquakes coincides with the area of highest temperature geothermal activity (> 340°C; Bjarnason & Ólafsson, 2000). At the western part of the caldera, high-frequency earthquakes (4–10 Hz with magnitude < 3), are located beneath the most recent eruptive sites; these earthquakes have been related to a brittle failure of the volcanic edifice (Einarsson, 1991; Lippitsch et al., 2005; Soosalu & Einarsson, 1997). Seismicity studies reveal a spherical aseismic volume (void of earthquakes) with center at 8-km depth and a diameter of 4 km (Soosalu & Einarsson, 1997, 2004) interpreted as a cooling, mostly solidified, magma volume. Geodetic studies show vertical deflation of ~12 mm/year in the west part of the volcano caldera (Scheiber-Enslin et al., 2011), also suggesting a magma chamber contracting due to a decrease of temperature.

While most of the cited deformation and seismic studies indicate the presence of a hot magma chamber feeding Torfajökull's geothermal area, one of the largest in Iceland, no seismic imaging study has been performed to confirm or contradict previous observations. Torfajökull's restlessness, the extensive area of high temperatures, and peculiar tectonic setting are ingredients for a potential eruption. Insights on Torfajokull's

magmatic plumbing system could be obtained from seismic imaging. An attractive alternative to the expensive active-source reflection seismics and to the nonoptimal spatial distribution of events for earthquake tomography is seismic interferometry (SI) with ambient noise (e.g., Draganov et al., 2007; Larose et al., 2005; Roux et al., 2005; Ruigrok et al., 2011; Shapiro & Campillo, 2004; Sabra et al., 2005a; Shapiro et al., 2005). The concept of SI was first proposed in the exploration community for 1-D media (Claerbout, 1968) and later extended for arbitrarily heterogeneous 3-D media (Wapenaar, 2004). From the wide range of SI applications, a very popular application is the retrieval of surface waves from cross correlation of ambient noise. SI with ambient noise for retrieval of surface waves is considered consistent with the spatial autocorrelation method (Aki, 1957, 1965) as shown by Yokoi and Margaryan (2008). The comparative study of the two approaches by Tsai and Moschetti (2010) also suggests that the results from each technique can be used in the other. The subsequent application of SI, tomographic inversion to obtain phase velocity maps, and the frequency-to-depth inversion is called ambient noise tomography (ANT). This results in a 3-D velocity model. ANT has been used to image the Earth's subsurface over large areas (e.g., Bensen et al., 2008; Kang & Shin, 2006; Sabra et al., 2005b; Villasenor et al., 2007; Yang et al., 2007; Yao et al., 2006), and on a local scale to image volcanic magmatic systems (e.g., Brenguier et al., 2007; Behr et al., 2011; Jaxybulatov et al., 2014; Luzón et al., 2011; Masterlark et al., 2010; Mordret et al., 2014; Nagaoka et al., 2012; Stankiewicz et al., 2010; Villagómez et al., 2011).

In this paper, we create the first image of Torfajökull's magmatic plumbing system with ANT. With the present study we aim at imaging Torfajokull's subsurface to understand if there are low-velocity zones beneath or outside the volcano caldera as result of an existing (molten or partially molten) magma chamber. Given the relatively short time acquisition of the seismic network for passive seismic purposes, we follow a methodology that aims at retrieving accurate surface wave phase velocity estimations for tomographic inversion, as well as to control the quality of the inversion results.

2. Retrieval of Surface Waves From Ambient Noise

2.1. Preprocessing of the Ambient Noise

We used 22 out of the 30 Güralp 6TD seismometers initially installed around and inside Torfajökull caldera (Figure 2 Soosalu et al., 2006) in the summer of 2005 (station coordinates and gathered data listed in the supporting information). Even though most of the seismometers were reported to have 100% data recovery, 7 out of the 30 stations had intermittent operation periods (starting and stopping at irregular intervals), and were reported to have GPS clock timing errors. At a later stage, we also excluded station STRU from our processing because of unreliable cross correlations. Therefore, to avoid gaps during data acquisition, we use the vertical component of the 22 selected stations simultaneously recording noise during a period of 100 days (approximately 14 weeks from 19 June till 27 September).

After the data acquisition, we preprocessed the recorded noise to prepare the waveforms for retrieval of surface waves by SI (Bensen et al., 2007) to e.g., remove trends, eliminate instrumental irregularities and thus to enhance the broadband character of the noise, and to suppress strong transient arrivals. The instruments have a sampling rate of 50 samples per second, thus, recording ambient noise up to 25 Hz. We remove the instrument response by complex deconvolution for all three components of the displacement to flatten the response down to 0.1 Hz.

We use time-domain normalization to down-weight high-amplitude arrivals (nuisance sources) in a continuous record by homogenizing the amplitudes over a predefined window length. The running-absolute-mean normalization described in Bensen et al. (2007), computes a running average of the absolute value of the waveform in a normalization time window. This normalized time window has a fixed duration of 2 s and weights the waveform at the center of the window by the inverse of the running average. The last step of the preprocessing is spectral normalization (or whitening) with the goal of broadening the ambient noise band for the cross correlations. The whitening is implemented through running-absolute-mean normalization in the frequency domain, with a window of 0.5 Hz.

2.2. Frequency Selection

2.2.1. Power Spectral Density

To select the bandwidth of the microseisms, we analyze the power spectral density (PSD) of the recorded signal, which shows where the average power is distributed as a function of frequency. We compare the measurements on stations spatially well spread over the seismic netwok with global measurements of

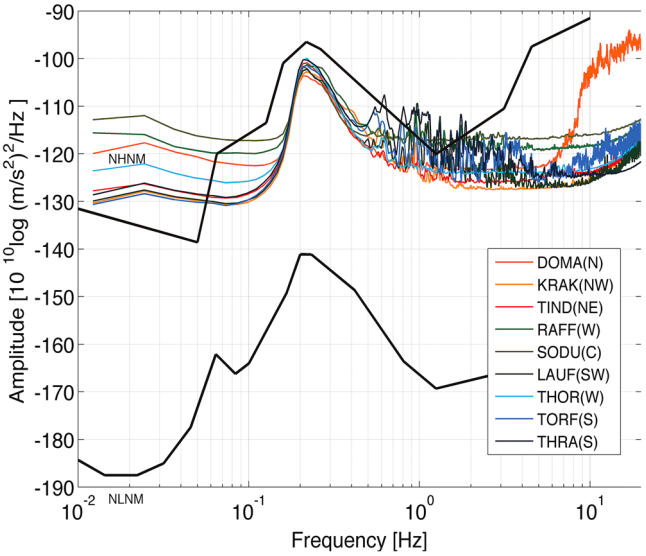

Figure 2. Variation of the power spectral density at the different selected stations for the day 220 (for station locations see Figure 1). Orange to red colors represent the northernmost stations. The stations located in the middle of the array are shown in green and the southernmost stations in blue, respectively. The black lines show the lower and upper limits given by the NLNM and NHNM models. NLNM = New Low Noise Model; NHNM = New High Noise Model.

ambient noise. We compute the PSD of the selected stations and compare the PSD with the models obtained by Peterson (1993), the NLNM (New Low Noise Model) and NHNM (New High Noise Model). Figure 2 shows the variation of the amplitudes in different frequency bands for nine stations on the edges and one in the middle of the seismic network for the day 221 of the year.

The PSD of all the analyzed stations follows the same trend as the models except for frequencies below 0.1 Hz, at which frequency the instruments rapidly lose their sensitivity. The recorded noise is closer to the NHNM indicating that the area is dominated by a high-noise level within almost all frequencies, as would be expected given the proximity to the ocean. The amplitudes between 0.1 and 1 Hz follow the NLNM and NHNM models trend, reaching a higher power spectrum peak at the double-frequency microseism (Haubrich et al., 1963). Substantial changes in the amplitude values of particular stations occur close to 1 Hz and above. Two stations (TORF and THRA) reach a peak of noise around 2 Hz which could be due to local geological features, perhaps connected with the local history of volcanic activity. From approximately 8 Hz to the maximum recorded frequency (25 Hz), stations DOMA, KRAK, and RAFF exhibit higher levels of energy. At station DOMA this is probably related to car traffic given the proximity to local roads. At stations KRAK and RAFF it might be caused by earthquakes, which are not included in the NHNM model.

2.2.2. Spectrogram Analysis

For an overview of the distribution of the noise in frequency and time, we compute the PSD of the whole time period for one station located in the center of the array (station JOKU). We divide the selected time period into windows of 5 min and then compute the PSD using the ensemble average for different segments of 11 shorter time windows. The spectrogram for JOKU station is shown in Figure 3. We identify two bandwidths: one between 0.1 and 0.5 Hz (the band) and the other between 10 and 25 Hz that exhibit a consistent presence of high-amplitude noise

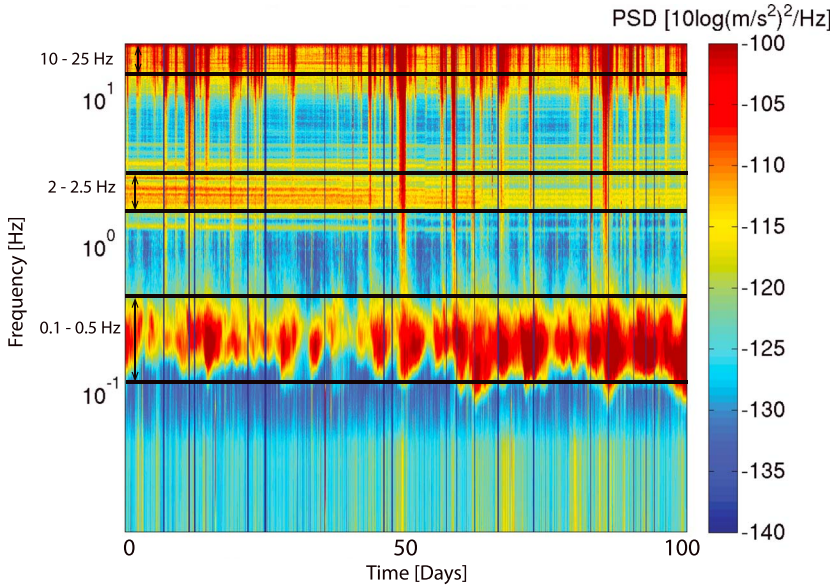

Figure 3. Spectrogram for JOKU station for the whole recording period (100 days) after removing the instrument response. We recognize three frequency bands with higher power identified by the horizontal black lines. Hours without data result in vertical blue lines spanning the entire frequency range.

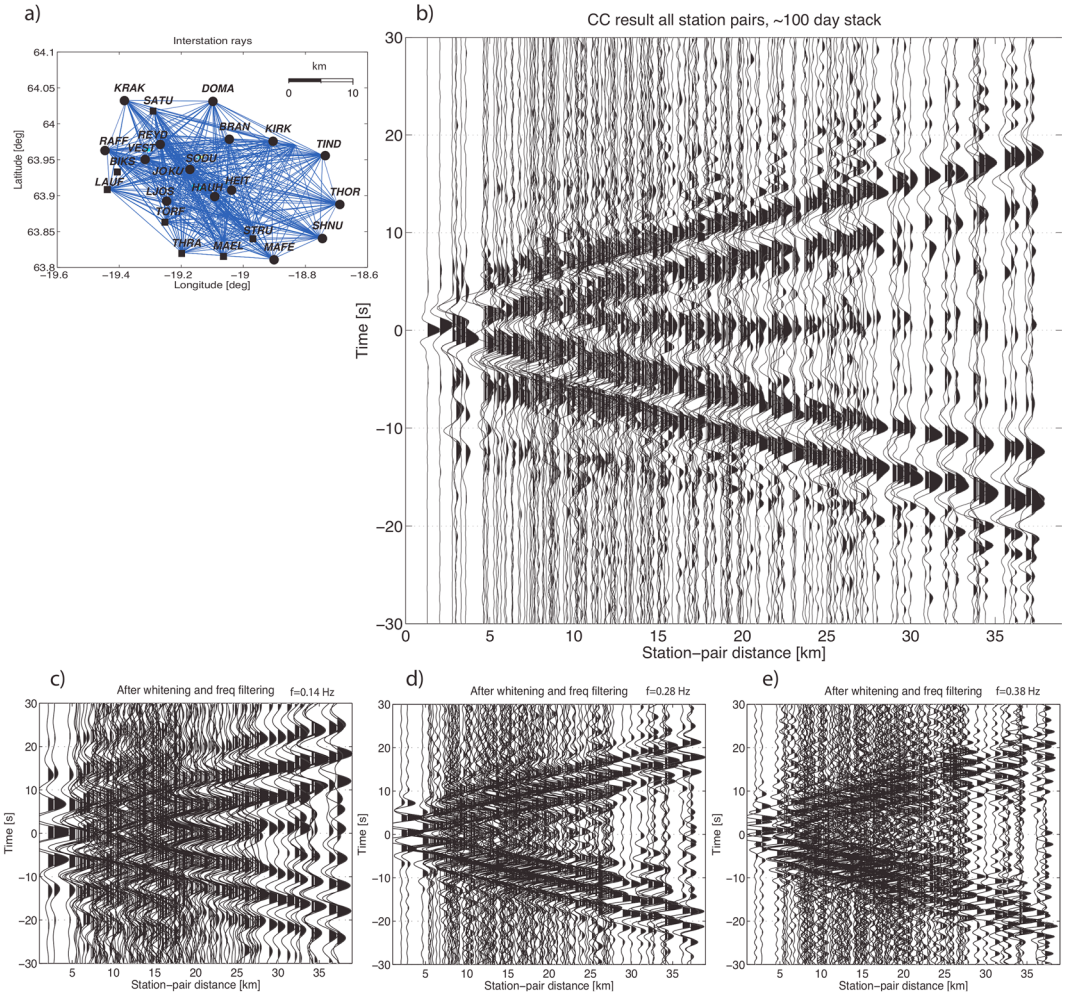

Figure 4. (a) Combinations of all station pairs for retrieval of surface wave arrivals. (b) The retrieved surface wave arrivals at positive and negative times in the frequency band between 0.1 and 0.5 Hz. The abscissa represents the station pair distance considering R the vector of distances between each station pair sorted by its magnitude. The ordinate represents the time, positive and negative according to the direction of surface wave propagation. (c, d, and e) The retrieved surface wave arrivals separated into three narrow frequency bands centered around 0.14, 0.28, and 0.38 Hz, respectively.

throughout the recording period. There is a third frequency band between 2.0 and 2.5 Hz which shows steady noise presence but with lower amplitudes.

We select the frequency band between 0.1 and 0.4 Hz not only because of its high PSD, but also because of the depth range of the surface waves to which these frequencies are sensitive. Within this frequency band, it is clear that the energy levels are significant. However, in time, the power does not always reach the upper and lower limits of this frequency band (close to 0.1 and 0.4 Hz), especially during the first half of the recording period. This means that the frequencies at the edge of the bandwidth might not have enough energy to retrieve acceptable surface waves. Nevertheless, at this selection stage, we are more permissive, and we select a frequency band comprising the detected limits of high energy. In the second half of the recording time period (from 20 August onward) the power is much higher than during the first half, most likely due to an increase of storms in the ocean, leading to an increase of microseism generation near the seabed.

2.3. Cross Correlation and Temporal Stacking

SI by cross correlation of the microseisms recorded at two stations aims at retrieving the coherent wavefield between this station pair. The collection of such retrieved wavefields between the different station pairs allows us to characterize properties of the medium between station pairs. By cross-correlating seismic observations at two receiver locations (e.g., x_A and x_B), we obtain a response at one of those receivers, x_B, as if

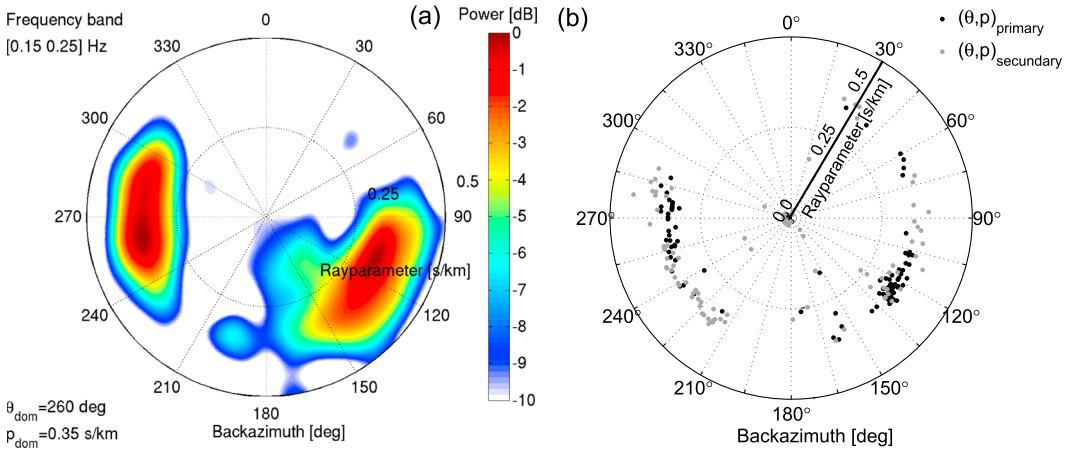

Figure 5. Beamforming analysis as a function of back azimuth and apparent velocity for approximately 100 days over the entire seismic network using a narrower frequency band (between 0.15 and 0.25 Hz). (a) Interpolation of the primary sources as a function of back azimuth and ray parameter. (b) Primary and secondary sources as a function of back azimuth and ray parameter.

there were a source at the other receiver x_A; this process is also called Green's function retrieval (Wapenaar, 2004). If we integrate over all sources along an integration boundary $\partial\mathbb{D}$, we will retrieve the Green's function $G(x_B, x_A, t)$ and its time-reversed version $G(x_B, x_A, -t)$. The Green's function contains the direct wave but also scattered waves (Wapenaar & Fokkema, 2006). This relation is given by the following equation:

$$G(x_B, x_A, t) - G(x_B, x_A, -t) \propto -\frac{\mathrm{d}}{\mathrm{d}t}\left(\oint_{\partial\mathbb{D}} G(x_B, x, -t) * G(x_A, x, t)\mathrm{d}^2x\right), \quad (1)$$

where $G(x_B, x_A, t)$ represent the Green's function between x_B and x_A (where t denotes time), while $G(x_B, x_A, -t)$ is its time-reversed version. On the right-hand side, the equation shows the cross correlations of wavefield observations at x_A and x_B integrated along sources at x along $\partial\mathbb{D}$. In the equation $*$ denotes the temporal convolution.

To retrieve the surface wave part of the Green's function, we bandpass filter the microseisms (from 0.1 to 0.4 Hz) of the ambient noise recorded during the selected 100 days, divide the ambient noise recorded at each station in portions of 1 hr and cross-correlate those portions for each station pair combinations. To recover the ballistic surface waves (BSW), we cross-correlate the vertical components of the station pairs, average the cross-correlated results over a long time period, and then we take the time derivative multiplied by −1 (equation (1)). In total, we apply SI to 253 station pairs (see Figure 4a).

We average (sum) the 1-hr correlations over the chosen 100 days of recordings. What we gain by the time averaging/stacking is a convergence of the retrieved signal to the surface wave part of the Green's function. In Figure 4b we see the results of averaging 100 days of cross correlations as a function of receiver-pair distance at positive and negative correlated lags. Each of the vertical lines corresponds to a retrieved trace between a certain station pair (Figure 4a).

The retrieval at positive times is an estimation of the fundamental-mode Rayleigh wave, whereas the result at negative times is an estimate of its time-reversed variant (Bensen et al., 2007). The arrivals at positive and negative time lags are not symmetrical indicating that the illumination is not isotropic: the illumination from one station to another is not the same as in the opposite direction. Figures 4c–4e show the retrieved Green's functions, band-pass filtered in narrower bands centered at 0.14, 0.28, and 0.38 Hz, respectively. The plots show well-retrieved results; however, for short intrastation distances, the retrieved arrivals at positive and negative time lags start interfering, resulting in less precise surface wave arrivals. We take this into consideration later when extracting the traveltimes from these waveforms.

2.4. Direction and Slowness of the Microseism Noise

SI requires an isotropic distribution of the illuminating sources to retrieve the complete Green's function (Roux et al., 2005; Weaver & Lobkis, 2004; Wapenaar, 2004). However, noise sources such as microseisms

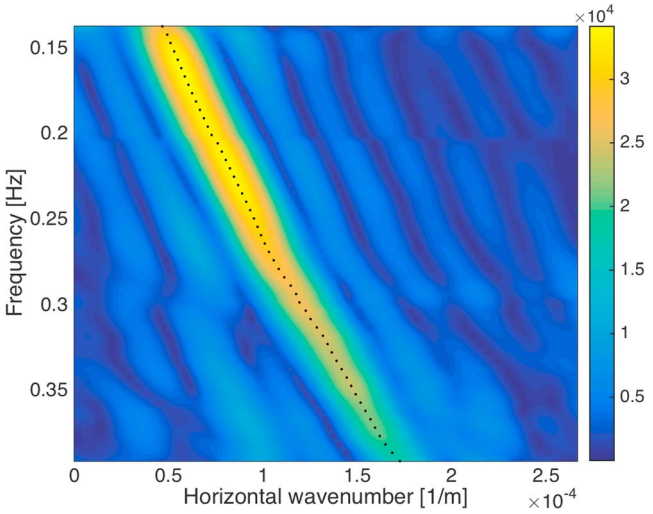

Figure 6. Frequency-wave number amplitude spectrum of the retrieved surface waves (Figure 4b). The black dots denote the wave number with the maximum amplitude picked for each frequency. The picked wave number-frequency function is used to derive an average dispersion curve over the array.

are usually characterized by a preferential source locations (Bromirski & Duennebier, 2002). We apply a beamforming analysis to determine the azimuthal distribution of the noise sources and also the apparent velocity of the microseisms surface wave noise. Whenever there is a lack of microseism noise traveling in that particular azimuthal direction, the beamforming results can additionally be used to discard station pairs oriented in the direction of erroneous retrieved BSW.

We apply beamforming directly to the stack of cross correlations over the entire 100-day period (Figure 5a).

The procedure for the beamforming can be found in, for example, Gerstoft and Tanimoto (2007), Lacoss et al. (1969), Rost and Thomas (2002), and Tanimoto and Prindle (2007), and the cross-correlation beamforming procedure is described by Ruigrok et al. (2017). The beam power results show the directionality of stronger noise sources, which are centered around the west and southeast (Figure 5a), traveling with apparent velocities near 2.8 km/s. When selecting the primary and secondary peak after beamforming of 1-day recordings (Figure 5b), we also found weaker sources. We identify predominant directions from back azimuth intervals within ∼ 15–35°, ∼ 60–75°, ∼ 90–180°, and ∼ 210–300°, showing roughly that no microseism noise is coming from directions between 300° and 15°. This shows anisotropic noise distribution, which means that for some station pairs reliable BSW would be retrieved only at positive or only at negative times. In Figure 5a there seems to be an illumination hole between ∼ 210° and ∼ 220°. However, Figure 5b shows that weaker sources are still covering these azimuths. We detect sufficient illumination, meaning that the BSW would be retrieved at both positive and negative times, or at least at one of the times, which can then be used as well. For this reason, after the beamforming analysis, we do not to exclude any station pair for the dispersion-curve extraction.

As Iceland is an island, it is expected to have ocean waves coming from all directions; however, storms, especially west and southeast of Iceland, could result in microseism noise predominantly from these directions. The sources of more powerful noise from westerly direction are likely to be related to the polar air effect over the ocean originating in Greenland (Båth, 1953) and eventually storms between Greenland and Iceland. The source of noise arriving from the southeast can be related to depressions heading for NW Europe. In both cases, the estimated directions of stronger microseism noise are consistent with the noise source locations from Stutzmann et al. (2012) for the period band 5–7 s of data acquired during summertime.

3. Velocity Variations at Depth From Surface Waves

3.1. Average Dispersion Curve

The average dispersion curve is estimated from the time-distance slope of the retrieved BSWs. The average phase velocity ($c(f)$) could be found in the time-space domain by filtering the data in a narrow band around f and picking a best fitting line through the BSW's and determine its slope: $c(f) = \mathrm{d}R/\mathrm{d}t$, where R is the receiver-pair distance. A more robust implementation is achieved in the wave number-frequency domain, where the phase velocity is estimated from the frequency-wave number slope: $c(f) = f/k(f)$, where $k(f)$ is the wave number function describing the BSWs.

The picking in the wave number-frequency domain follows the approach of the multichannel surface wave method (MASW) of Park et al. (1998, 1999). In this approach, the dispersion curve (phase velocity as a function of frequency) is extracted from the amplitude spectrum preserving the information about the phase spectrum (dispersion properties). Implementing a multichannel analysis has several advantages, mainly in effectively identifying noise that contaminates the estimation of fundamental-mode Rayleigh wave dispersion (higher-mode Rayleigh waves, refracted and reflected body waves, scattered and non–source-generated surface waves).

From the retrieved BSWs (Figure 4b), we take either the positive times, or the time-reversed negative times, dependent on the side with the highest signal-to-noise ratio. The resulting panel is transformed to the wave number-frequency domain. Figure 6 shows the amplitude spectrum.

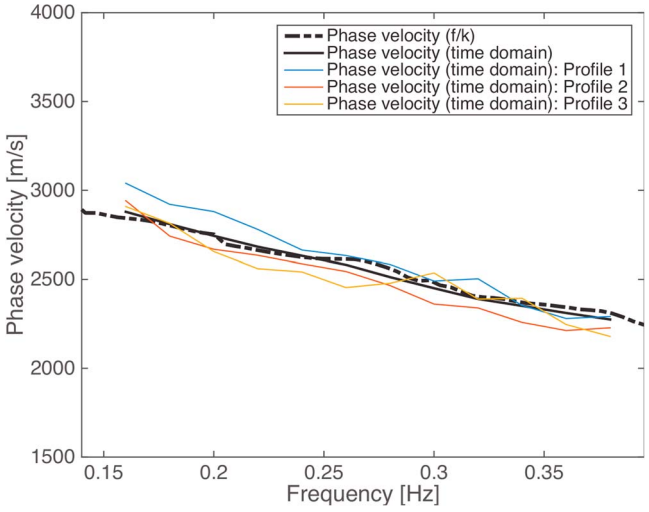

Figure 7. Average phase velocities over the seismic network. The dashed and continuous black lines are phase velocities from pickings in frequency and time domain, respectively. Colored lines are the phase velocity dispersion curves of three random station pairs.

For each frequency, the wave number with the maximum amplitude is picked, yielding the function $k(f)$ and the dispersion curve ($c(f) = f/k(f)$). Figure 7 shows the phase velocity dispersion curves for a three station pairs (colored lines). The black lines are the average dispersion as found by averaging over all station pair paths. Both the average dispersion as estimated in the time domain (black continuous line in figure) and the average dispersion as estimated in the frequency-wave number domain (black dashed line) show similar velocity variations. Moreover, the first-order similarity of both dispersion curves shows that the phase-correction term we use for the time-domain picks is a fair estimation.

The amplitude spectrum is not affected much by aliasing. Using 232 station pairs with maximum station pair distance R_{max} and minimum station pair distance R_{min}, the average spacing between subsequent station pairs is $dR = (R_{max} - R_{min})/231 = 153$ m. This spacing yields the following approximate Nyquist wave number: $k_{NY} = 1/(2dR) = 0.0032\ \mathrm{m}^{-1}$. k_{NY} is significantly larger than the extent of the wave number axis in Figure 6. However, the irregularity in station-distance distribution does result in spurious mappings of the BSWs to the frequency-wave number domain. In Figure 6, the aliased-like features can be identified as low-amplitude frequency-shifted repetitions of $k(f)$. There are no indications of higher modes or retrievals other than surface waves that are consistent over the entire array.

3.2. Path Dispersion

In the time domain, we extract the dispersion curve averaged over the paths connecting the different station pairs. The picks in the time-domain are performed in narrow frequency bands, between 0.12 and 0.44 Hz, with steps of 0.02 Hz. Assuming the filtered response to be monochromatic with frequency f_i (where $i \in [0.12,\ 0.4]$ with the defined 0.02 step), the time domain BSW is written as a phase-shifted cosine:

$$u(t, f_i) = \cos(2\pi f_i t - 2\pi R/c - \phi_{VS}), \tag{2}$$

where R is the distance between the two receivers, $c(f_i)$ is the phase velocity and ϕ_{VS} is the phase term of the virtual source.

The phase shift is composed of a distance term $2\pi R/c$ and a source term ϕ_{VS}. For perfect illumination, the phase of the virtual source (reconstructed source) is $\frac{\pi}{4}$. This additional phase term stems from the two-dimensional wave propagation of surface waves. For imperfect illumination and/or additional interference with spurious terms, ϕ_{VS} will be frequency dependent deviation from $\frac{\pi}{4}$. Lin et al. (2008) introduced the parameter λ to express the phase deviation due to imperfections and coined it the source phase ambiguity. λ and ϕ_{VS} are related as $\phi_{VS} = \pi/4 + \lambda$. In this manuscript, we use the symbol λ to refer to wavelength.

Isolating the phase velocity from expression 2 yields

$$c(f_i) = \frac{R}{t(f_i) - \phi_{VS}/(2\pi f_i)}. \tag{3}$$

Hence, we estimate the dispersion curve by first picking $t(f_i)$ from the bandpass filtered BSW's and subsequently correcting for the virtual-source phase term.

To pick $t(f_i)$, we use the guidance from the average phase velocities using the MASW algorithm to circumvent timing mismatches due to the interference of retrieved arrivals at positive and negative times and to avoid picking at an incorrect cycle. Figure 8 (top row) shows examples of retrieved BSWs bandpass frequency filtered using narrow bands around f_i. Due to the narrow band remaining, the signal is still somewhat localized in time. For most frequencies and station pairs, $t(f_i)$ corresponds with $t_{max}(f_i)$, the time at which the maximum amplitude occurs. However, sometimes a velocity closer to the MASW estimate is obtained by picking the next cycle: $t(f_i) = t_{max}(f_i) + 1/f_i$. In theory, also the cycle before t_{max} could lead to a velocity closer to the MASW estimate. This case does not occur for this data set probably related to the fact that reducing $t(f_i)$

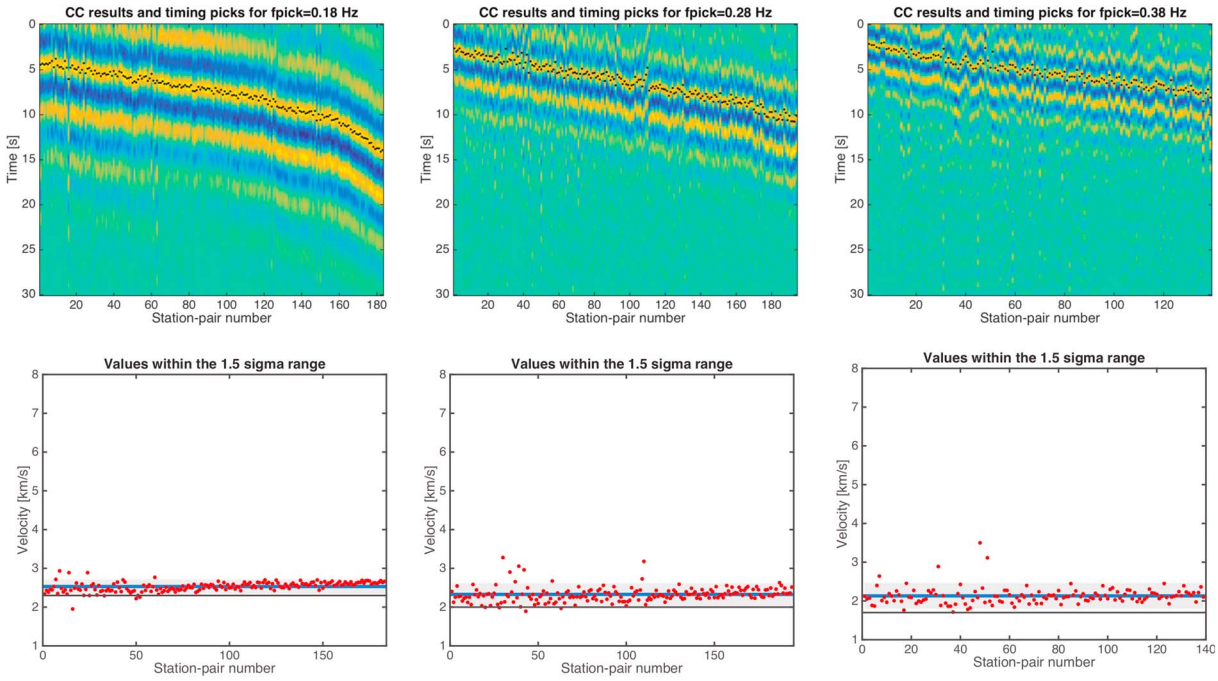

Figure 8. (top row) Traveltime picking for the frequency values 0.14, 0.28, and 0.38 Hz. The color bar indicates the coherence of the retrieved surface waves, and the black dots are the actual pickings. (bottom row) Final velocity values obtained from the picked times. We select for the tomographic inversion only those values that fall inside the 2σ interval (gray zone) from the mean value (the blue line).

in equation (3) leads to significantly higher velocities for the small station distances involved in this data set ($R < 40$ km). The traveltime picks are made after taking the time derivative of the cross correlations multiplied by -1 (equation (1)). This differentiation is required to interpret the interferometric result as part of a Green's form.

The quality of the retrieved BSW degrades when the interstation distances (R) are too short or too long (Figure 4). For short distances there is interference between acausal and causal times and therefore we cannot pick accurate timing. Some authors define this minimum distance as $3\lambda_{f_i}$ (Bensen et al., 2007), others as $2\lambda_{f_i}$ (Shapiro et al., 2005). At larger distances, especially when the wavelength of the surface wave is shorter, direct waves start interfering with scattered waves. The maximum distance between station pairs should also be set, as such scattered-wave arrivals complicate the pickings of BSW at larger distances. The thresholds we use to discard station pairs based on the minimum and maximum interstation distances ($R_{i,\min}$ and $R_{i,\max}$) are, respectively:

$$R_{i,\min} = \frac{2}{3}\lambda_{i,0}, \tag{4}$$

$$R_{i,\max} = 2.8\lambda_{i,0}, \text{ with } \lambda_{i,0} = \frac{v_{i,0}}{f_i} \tag{5}$$

where $0.12 <= f_i <= 0.4$ Hz with a step of 0.02 Hz, $v_{i,0}$ is the average reference velocity for each frequency value, and $\lambda_{i,0}$ is the wavelength obtained from the average velocity, per frequency value. Here, we are less conservative in defining the minimum distance than previous studies. However, we select only retrieved surface waves with high SNR and no serious interference to allow accurate traveltime picking. The maximum distance was defined empirically by visual inspection of the distance where a clear identification of the direct wave becomes problematic. We select either the causal or acausal side, based on the side with the highest amplitudes. We make this choice before taking the time derivative of the retrieved SI results multiplied by -1.

In our data set, we restrict the path dispersion estimation to waves that travel in less than three cycles from source to receiver (equation (5)). With this restriction, it is unlikely that a wrong cycle is chosen when using the MASW velocity as a guide. For data sets with larger station distances and/or for higher frequencies, there is a risk of underestimating or overestimating the path dispersion if our approach would be used.

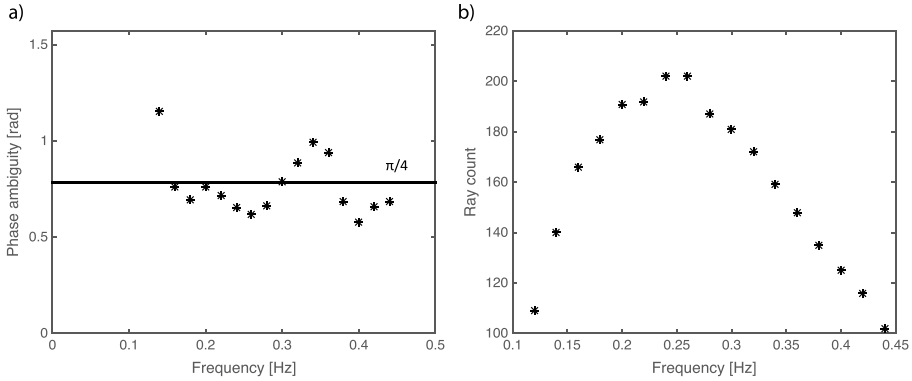

Figure 9. (a) Estimated phase term of the virtual source (ϕ_{VS}) per frequency. The phase term of the virtual-source values are close to $\frac{\pi}{4}$. Frequencies 0.3 and 0.32 Hz show the second highest variation from the expected $\frac{\pi}{4}$ value. (b) Number of raypaths per frequency. The lowest number of raypaths is, as expected, at the limits of the frequency band from 0.12 to 0.44 Hz.

Finally, we do an additional outlier check as a way to determine outliers that are caused by poorly retrieved fundamental-mode Rayleigh wave or by an interference of retrieved fundamental-mode Rayleigh waves with other retrieved waves. While picking the traveltimes, we discard values falling outside the 2σ deviation from the mean. In Figure 8 (top row) we show the picked points (on either the causal or time-reversed acausal interferometric result) for the different station pairs for the same three frequency values shown in Figure 4. In Figure 8 (bottom row) we show the picked traveltime values converted into velocities using the intrastation distances. Below each picked point figure, we show the corresponding 2σ confidence interval around the mean velocity value per frequency band. After removing the outliers and applying the correction with the theoretical value of $\pi/4$, we obtain a dispersion curve for each station pair.

3.3. Source Phase Estimation

As a quality measure of the illumination, we make an estimate of the frequency-dependence of the virtual-source phase term $\phi_{VS}(f_i)$ (equation (2)). For a given frequency f_i, we plot the traveltime picks $t(f_i)$ for multiple station pairs as a function of distance and fit a linear function through the points. From the intersection of this line with the time axis $t_o(f_i)$ we estimate the average virtual-source phase term:

$$\phi_{VS} = 2\pi f_i t_o. \tag{6}$$

Phase values closer to $\pi/4$ indicate a higher quality of the retrieved surface waves and time picking for the respective frequency. In Figure 9 we show the estimated virtual-source phase per frequency (a) as well as the number of raypaths per frequency (b). The latter parameter is largely governed by the wavelength-based thresholds (equations (4) and (5)). By analyzing the two graphs, we can see that ϕ_{VS} for 0.12 Hz is more than double the expected value. For 0.4 Hz the number of raypaths starts to decrease, and to be conservative at the limits of the frequencies, so we decided to select a narrower frequency band of the picked traveltimes, $0.16 \leq f_i \leq 0.38$ Hz, in the subsequent tomographic analysis.

Lin et al. (2008) describe an alternative way to estimate the source phase $\lambda = \phi_{VS}(f_i) - \pi/4$. Their method is based on comparisons of traveltimes of station triples that are nearly aligned along the same great circle. The advantage of our method is that such station triples do not need to be present. Our method can be implemented for more arbitrarily array configurations. The requirement, though, is that for one f_i enough station pairs are present to confidently fit a time-distance curve.

3.4. Azimuthal Velocity Variations

Using the estimated traveltimes, we check the azimuthal velocity variations to identify trends or possible inconsistencies of estimated velocities in frequency and direction. Figure 10 depicts the derived azimuthal velocity variation. There is a trend, over the complete frequency range, of the highest speeds being near 40° and near 220°. The lowest velocities are between 100° and 170°. Note that these azimuths are close to the ranges where we had lower illumination (section 2.4) due to weaker sources (Figure 5b). Nevertheless, because the source-phase estimation indicates that there was sufficient illumination (section 3.3), it is more

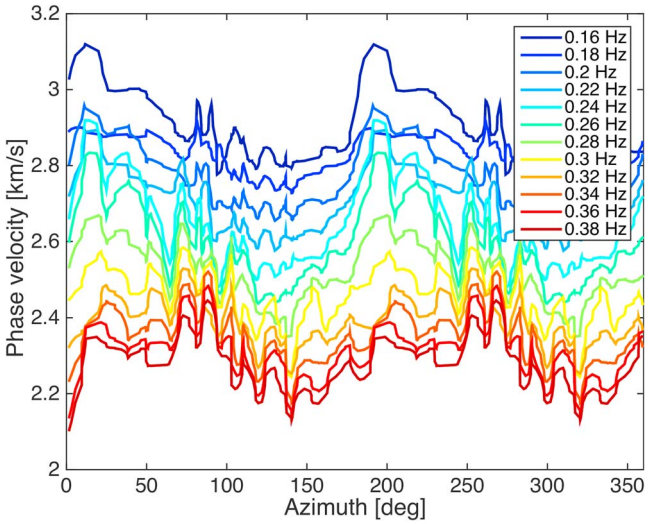

Figure 10. Variation of the phase velocity with azimuth and frequency.

likely that possible anisotropy causes the azimuthal dependence in the velocities. The inferred fast axis (30°) corresponds well with the strike of the rifting as well as to the orientation of erupted lavas on a NE-SW fissure swarm (Ivarsson, 1992).

4. Tomography

To constrain the geometry and location of the magma system beneath Torfajökull volcano, we invert the traveltimes between each station pair to estimate surface wave velocity variations. The following forward problem is inverted:

$$\begin{bmatrix} tt_1 \\ tt_2 \\ \vdots \\ tt_{n-1} \\ tt_n \end{bmatrix} = \begin{bmatrix} s_1 \\ s_2 \\ \vdots \\ s_{n-1} \\ s_n \end{bmatrix}^T . \begin{bmatrix} l_{1,1} & l_{1,2} & \dots & l_{1,j-1} & l_{1,j} \\ l_{2,1} & l_{2,2} & \dots & l_{2,j-1} & l_{2,j} \\ \vdots & \vdots & \vdots & \vdots & \vdots \\ l_{k-1,1} & l_{k-1,2} & \dots & l_{k-1,j-1} & l_{k-1,j} \\ l_{k,1} & l_{k,2} & \dots & l_{k,j-1} & l_{k,j} \end{bmatrix} \tag{7}$$

where tt_n ($n = 1, .., N$) are the traveltimes previously determined for each ray, $l_{k,j}$ ($k = 1, .., N; j = 1, .., M$) is a matrix of the path length of the kth ray in the jth grid cell.

This problem formulation is solved in a linear least squares context $d_f = G \cdot m + e$, where d_f is the traveltime vector per frequency, G is the design matrix relating slowness with the traveltimes, m contains the model parameters, and e is the noise contaminating the measurements. For each frequency value, we built the $N \times M$ design matrix G (of full rank equal to N), where N represents the number of raypaths found for a certain frequency (Figure 9) and M is the number of grid cells. The number of nonzero elements of the design matrix is dependent on the number of raypaths previously selected. The model parameters are estimated independently for each f_i.

As we are interested in slowness perturbation with respect to a background model, we first remove the velocity at each frequency by

$$\Delta d_f = d_f - G_f . s_{0,f}, \tag{8}$$

where Δd are the traveltime estimated with respect to the reference velocity at frequency f (the reference slowness $s_{0,f}$). The reference velocity we use in this formula is not the velocity derived from the dispersion curve but the average velocity from the picked traveltimes.

4.1. Tikhonov Regularization

We regularize the ill-conditioned inversion problem by adding a new term to the least squares problem (Tikhonov, 1963):

$$min_x\{||d - Gm||^2 + \mu||m||^2\}, \tag{9}$$

where $\mu \geq 0$ is the regularization parameter, also known as the damping factor. The accuracy of the inversion procedure is directly affected by choice of the regularization parameter (Kusche & Klees, 2002). If μ is too small the solution is contaminated by the noise as it overfits d, if μ is too large, the solution becomes very smooth, and it is a poor approximation of m. To choose a reliable smoothing parameter for regularization, we use the cross-validation methodology (Golub et al., 1979). A different smoothing parameter is selected per frequency value as the raypaths per frequency are inverted independently.

4.2. Checkerboard Tests

We perform a checkerboard sensitivity test (Lévêque et al., 1993) to check the ability of our inversion methodology to solve the geometric details for the chosen grid size of 4 km. First, we create a regular 2-D checkerboard of opposite polarities with perturbations over an 8-km grid and with velocity perturbations in the same range as the data. Then we simulate the same number and combination of raypaths as used for the tomographic inversion. We also add noise to the modeled surface wave arrivals to simulate realistic errors during traveltime picking. Finally, we invert the simulated data applying Tikhonov regularization with the

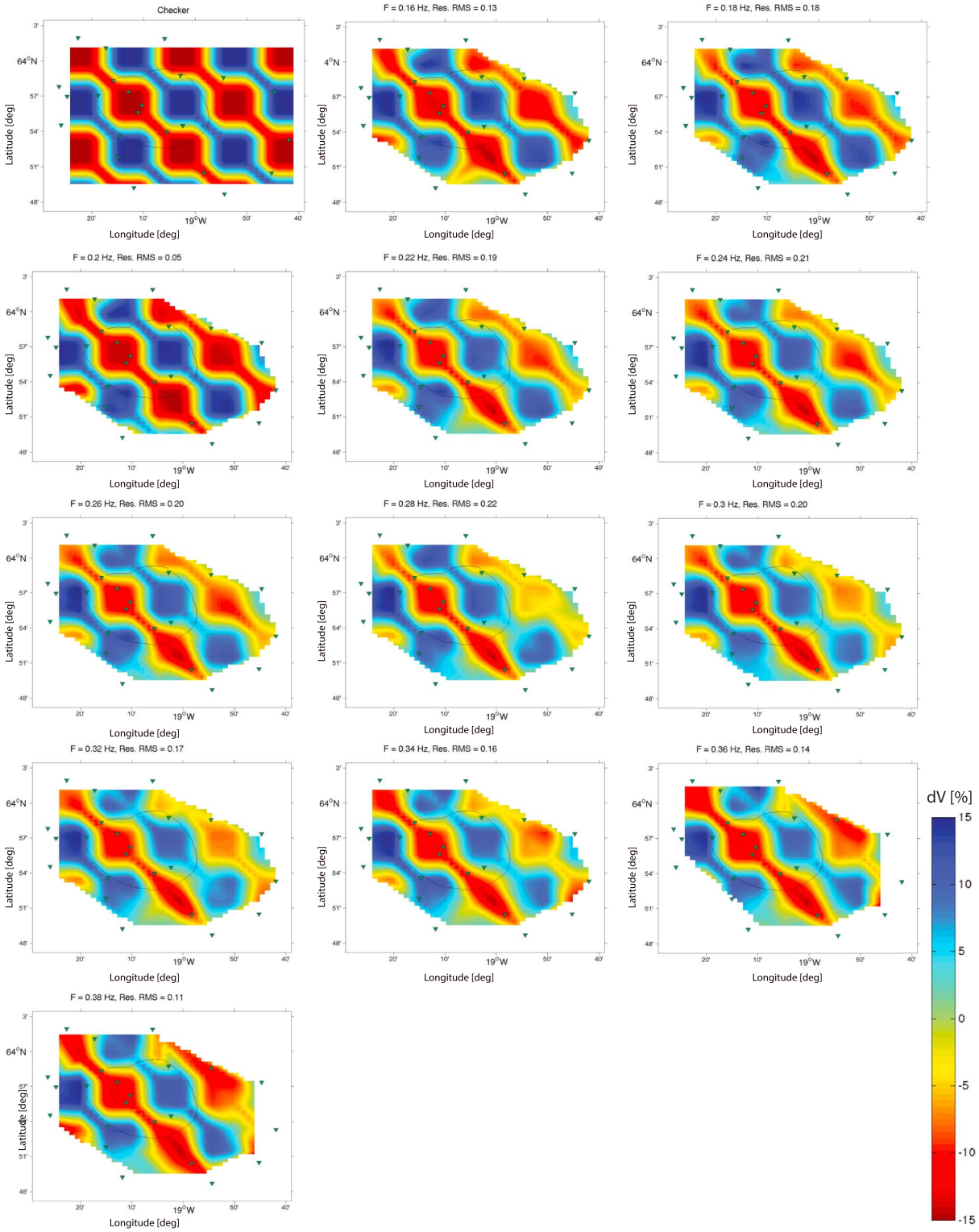

Figure 11. Checkerboard test results per frequency. Green triangles locate the stations and the black line the caldera, both at the surface.

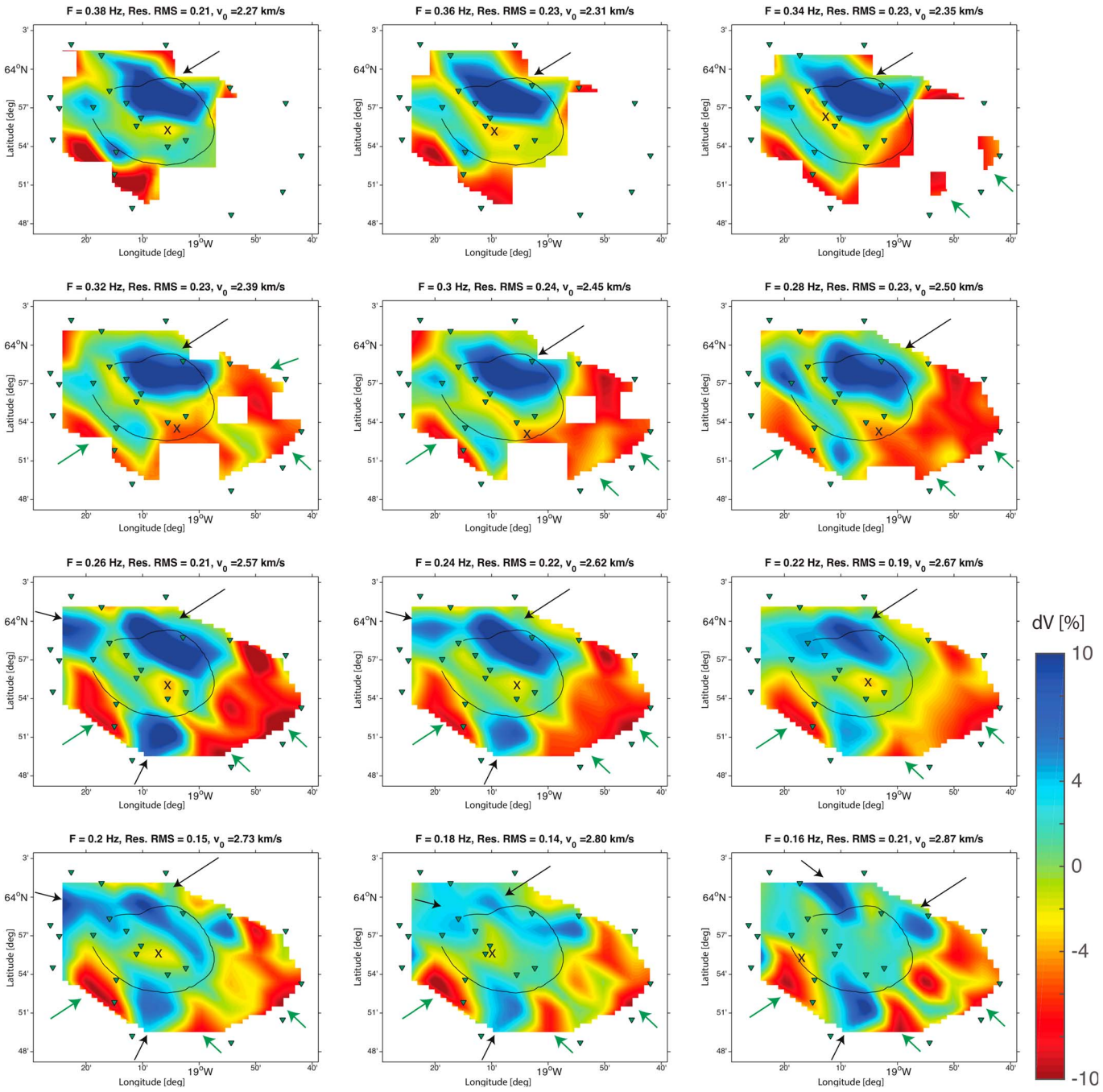

Figure 12. Tomographic results for different frequency values representing variations of velocity with respect to a reference velocity. Blue and red denote higher and lower velocities, respectively. The black line indicates the caldera outline; the green inverted triangles are the locations of the seismic stations at the surface.The green and black arrows indicate low-velocity and high-velocity features, respectively. The crosses locate the areas of lower velocities within the caldera outline. White areas locate grid cells where the number of raypaths is not enough to estimate a constrained velocity variation.

previously estimated smoothing parameter (μ) per frequency. Figure 11 shows the simulated checkerboard velocity model and tomographic results.

The simulated inversion can fully recover the principal geometry of the perturbed model, especially for frequency values used in this study (between 0.16 and 0.38 Hz), indicating a good number of simulated raypaths and distribution of receivers. Because we impose a regularization (smoothing) parameter that decreases the variability of the velocity values, quantitatively, the inversion result does not fully describe expected velocity variations.

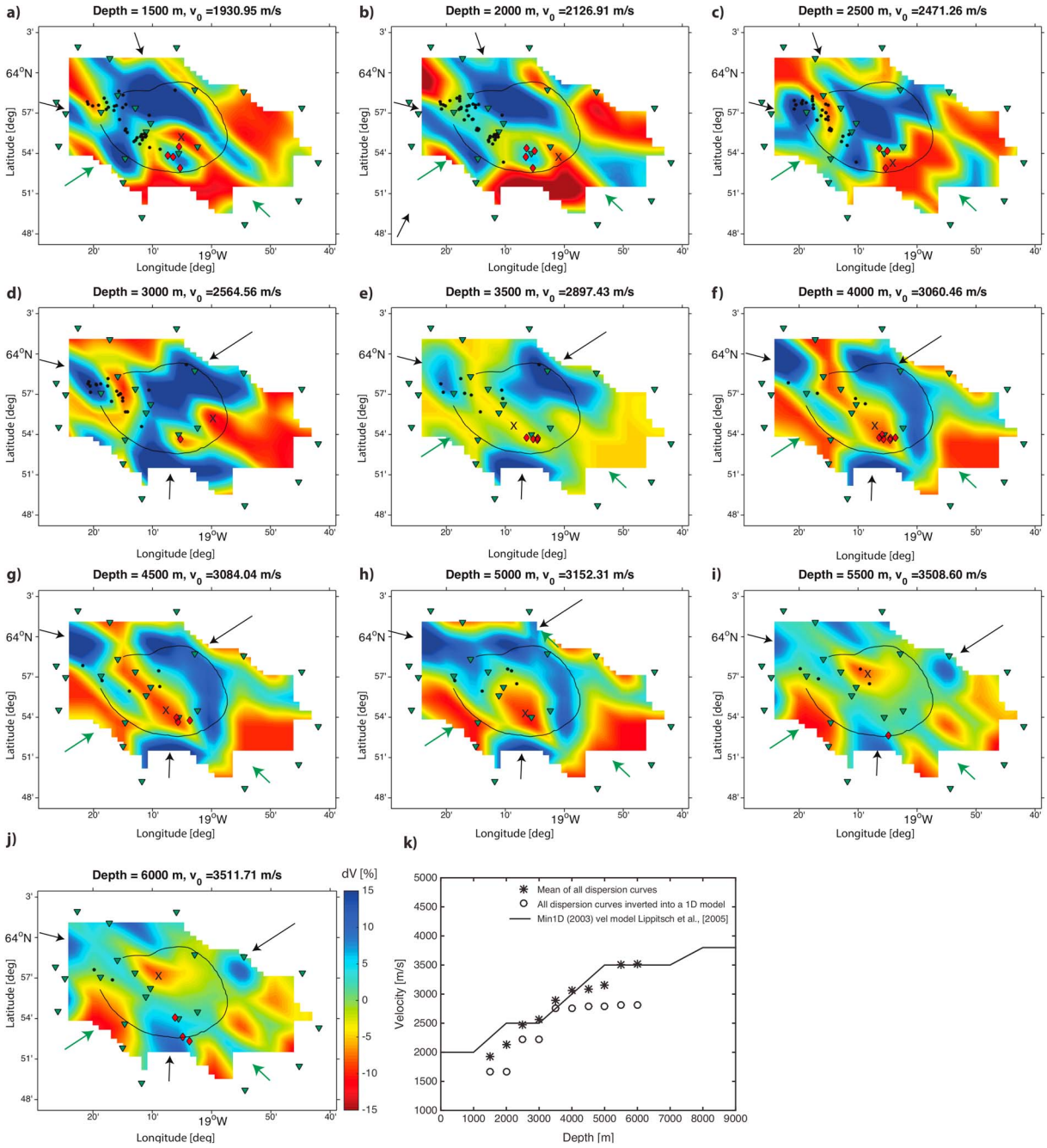

Figure 13. Three-dimensional shear velocity model of the waves velocity variations with respect to an average 1-D velocity model at depth. Blue and red denote high and low velocities, respectively. The filled black line represents the caldera outline at the surface; the green inverted triangles are the locations of the seismic stations at the surface. Black dots represent high-frequency earthquakes, while red diamonds low-frequency earthquakes. The green and black arrows indicate low-velocity and high-velocity features, respectively. (k) The average velocity profiles at depth from three sources. The average of all the grid cells per depth, which is the reference average for which the anomalies are plotted (asterisks). A velocity model derived using all the dispersion curves and the adopted parametrization (circles). And the 1-D *S* wave velocity profile from Lippitsch et al. (2005) over Torfajökull.

5. Results

5.1. Surface Wave Tomography

Using Tikhonov regularization, we invert the picked traveltimes of the retrieved ballistic Rayleigh waves for phase velocity variations at depth. Prior to the depth inversion, we first invert each frequency independently over a 4- by 4-km grid, using grid cells crossed by at least six raypaths. We choose this resolution based on a compromise between a desirable high spatial resolution and a threshold of at least five raypaths per grid cell. Figure 12 shows the Rayleigh wave phase velocity variation maps for different frequencies.

The inverted results show velocity variations that reach up to 15% from the average velocity for each frequency. For display purposes, we plot the results on a scale of −10% to 10% to highlight anomalies above 5% deviation from the mean velocity. The velocity deviations vary remarkably smooth as a function of frequency even though each frequency is inverted individually, indicating solid traveltime picks and stable inversion results. In the current inversion implementation we did not take into account anisotropic variations nor ray bending for phase velocity estimation; therefore the results could eventually be improved.

5.2. Three-Dimensional *S* Wave Velocity

With the following procedure, we produce a 3-D shear-velocity model (Figure 13 displayed with variations between −15% and 15%) from the phase velocity maps. Per grid cell, we build a dispersion curve using the phase velocity estimated from the 2-D tomographic results at different frequencies (Shapiro et al., 2004). We invert a total of ∼50 dispersion curves individually using the neighborhood algorithm (NA) in a Monte Carlo approach, described by Sambridge, (1999a, 1999b), later implemented and improved by Wathelet (2008).

The approach follows a stochastic searching method assuming the dispersion characteristics of surface waves are mostly dependent on layer parametrization (depth, thickness, and densities) and body wave velocities (V_p and V_s linked by Poisson ratio). The optimum model is the velocity-depth model for which the forward modeled dispersion curve has a minimum misfit with the measured dispersion curve (Wathelet et al., 2004).

As result of the smoothness in the forward computation of the dispersion curves, it is difficult to identify sharp velocity jumps, for example, when stiff rocks are juxtaposed with low-velocity zones (LVZ) at depth. To tackle the identification of complex boundaries we tried to detect different layers by first parameterizing the model in three layers without fixing depths. The boundary layer does not differ much between nearby grid cells, but change between grid cells where the frequency dependent tomographic results (Figure 12) show contrast between velocity variations. This confirms irregular boundary layers within the area of interest.

We parameterize our model in five fixed horizontal layers allowing the V_p and V_s velocities to change with depth within these layers. We assign an ample interval for the V_p input velocities (∼4,000 m/s between the lower and upper bounds) allowing a higher range of solutions and because the presence of stiff rocks can influence V_s as reported by Wathelet (2008). We assume a fixed density of 2,600 kg/m^3, a varying Poisson ratio between 0.24 and 0.28, and estimate the *S* wave velocities from two independent runs with different boundary layers. We run the model first for depths limits between 1.5 and 5.5 km and then for depth limits between 2 and 6 km, both with 1-km vertical resolution. For each of the runs, the methodology we follow is similar to that of Kao et al. (2013) and Mordret et al. (2014). Per grid cell, from a total of ∼30,000 models, we choose the depth model with a minimum misfit. In Figure 13 we show the variations of the *S* wave velocity with reference to a 1-D velocity model (the mean of the estimated velocities per depth) for the two model runs (a, c, e, g, and i are the result of the first run and b, d, f, h, and j of the second run). The reference 1-D velocity model (asterisks in Figure 13k) is the average of all the grid cell inverted models. To check the quality of the reference velocity model, we compare two other 1-D *S* wave velocity models. The first is the model with the minimum misfit using all the dispersion curves as targets with corresponding parameter space and inverting for a single average dispersion curve (Figure 13k identified with circles). The second is the 1-D velocity model obtained by Lippitsch et al. (2005) for the same area with a different seismic campaign (Figure 13k identified by the black line). The first shows no difference between the two parameter spaces, meaning that the model derived with the minimum misfit using all the dispersion curves as targets is exactly the same for the two model runs. This model also has lower estimated velocities than the mean of all the dispersion curves for all depths. The adopted reference velocity model (Figure 13k identified by asterisks) shows a remarkable fit for most of the depths with the 1-D model of Lippitsch et al. (2005).

Figures 14a and 14b depict the standard deviation of the estimated velocity from the best 10% models at each grid cell. The maximum velocity standard deviation detected is of 146 m/s at 2.5-km depth (Figure 14a) in an isolated pixel in the periphery of the model. This corresponds to ∼5% from the mean velocity at the same depth. Most of the standard deviation values are in the order of 20 m/s, approximately between ∼0.5% and ∼1% depending on the analyzed depths. The standard deviation from the best In the same figure we show an example of a dispersion curve with the corresponding 30,000 models, misfits and the final selected model with the minimum misfit. The dispersion curve that serves as example is the grid cell identified in (a) by a red vertical line.

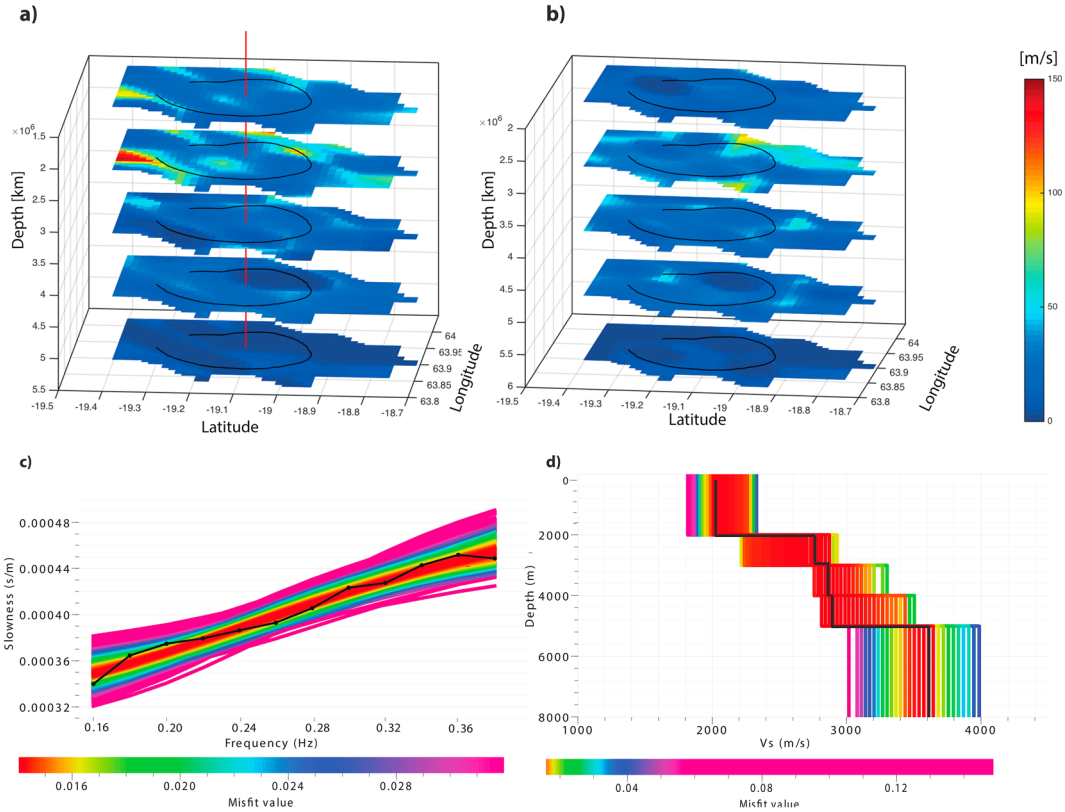

Figure 14. (a and b) Standard deviation of the velocity estimated from the 10% models with lowest misfit for the depths [1.5, 2.5, 3.5, 4.5, and 5.5 km] and [2, 3, 4, 5, and 6 km], respectively. (c and d) The input dispersion curve and depth velocity of a grid cell (red line in a) with the corresponding 30,000 models and misfit. The black line in (c) and (d) locates the model with minimum misfit.

6. Discussion

6.1. Quality Control

The quality of tomographic inversion depends on the three fundamental properties of the data and their interdependence: the noise in the observations, the seismic network configuration and the model resolution.

The way we deal with noisy observations is by rejecting them throughout the whole processing chain. We select the microseismic frequency band with the highest SNR. After the cross correlation, we make sure we have used high-amplitude microseisms noise to retrieve coherent causal or acausal surface waves. Using the most reliable waveforms from the cross correlation, we perform the traveltime picking avoiding too long or too short intrastation distances (equations (4) and (5)). We compute an average dispersions curve before picking station pair dispersion curves. In an initial approach, we use MASW to deal with a suboptimal seismic network configuration toward seismic tomography applications (our array is slightly skewed in the NW-SE direction), as well as to address local noise sources, scattered waves and correct phase-ambiguity estimation. In a second approach, we use MASW results to guide the time-domain picking. As we see a degradation of the dispersion measurements related to the spacing of the array above and below certain frequencies, we narrow the frequency band used from 0.1–0.4 to 0.14–0.38 Hz. After the traveltime picking, we only select the velocity variations within 2σ from the mean to avoid noisier observations and picks made on an erroneous cycle. During the traveltime picking process, we estimate the surface wave phase velocity term from the estimated pickings instead of assuming the derived $\pi/4$ value (Snieder, 2004). In this way, we have a measure to validate, using all the traveltimes per frequency, how the estimation reproduces the expected $\pi/4$ phase shift. We remove the frequency values for which this estimation is far from the expected value, for example for the traveltimes measured at 0.14 Hz.

The resolution of tomographic results depends primarily on the wavelength of the signal (v/f where v is the velocity of the seismic wave). At higher frequencies, the modeled results extract more detail, while at lower

frequencies, the results are smoother. The regularization during the inversion automatically deals with this as we can see that the results for lower frequencies are more smeared. The other parameter on which the resolution is dependent is the number of raypaths covering a particular area. We use a regular grid of 4 km, and the ray coverage was more than sufficient to invert slowness for this resolution, as shown by the checker-board test. The raypath count is much higher within the caldera outline indicating that the estimation is more redundant. Due to the number of raypaths, the degradation of the dispersion measurements and the performance of the checker-board for different depths, we decide to remove the edge frequencies (0.12, 0.14, and 0.40 Hz) for the inversion to *S* wave velocities as we have less confidence in the inverted results for these frequencies.

Because we are dealing with ambient noise interferometry, another component can worsen the quality of the traveltime estimation before inversion—the direction of the ambient noise with respect to the orientation of a station pair combination. We addressed the surface wave directionality topic in section 2.4, where it does not seem to be an issue for this data set.

6.2. Torfajökull's Magmatic System

We successfully identify velocity variations between approximately 1.5 and 6-km depth. We find two areas with velocity anomalies between −10% and −15% located in the eastern and southwestern investigation areas, outside the volcano caldera. These low-velocity anomalies are consistently present at depth in both frequency and depth domains (green arrows in Figures 12 and 13). In the eastern case, the velocity anomalies below −10% seem to be part of a larger hot body extending in the SE and SW direction. Even with a more demanding selection of the number raypaths at each grid cells (minimum of 10 raypaths per grid cell) at the edges of the horizontal layers, these low-velocity anomalies persist. Up to 4.5-km depth we identify velocity variations below −10% in the NW quadrant outside the volcano caldera. The detected below −10% anomalies may indicate the existence of warmer material for all the explored depths.

Beneath the volcano caldera we detect small areas with low-velocity anomaly reaching ∼ −6% variation at most of the frequencies (marked with crosses in Figure 12). Some of these features become more pronounced after the conversion from frequency to depth (Figure 13 marked with crosses). This occurs because some of the grid cells with the lowest velocities at the edges of the model are dropped out from the frequency to depth conversion because of information lacking at some frequencies. Even though the anomalies inside the caldera are less prominent than outside, the model is constrained by a higher number of raypaths. At shallower depths (up to ∼3-km depth), velocity variations down to ∼ −10% over small areas, may also indicate hot material, or possibly even the presence of small amounts of magma. These lower variations may be the origin of the high-temperature geothermal field at the surface (Bjarnason & Ólafsson, 2000) as the location of both correlates well. From 3.5 km to higher depths, we detect a low-velocity anomaly reaching between −10% and −15% variation beneath the volcano caldera (Figures 13e–13j) extending spatially in a NW-SE fashion. In the same figure we also plot the low and high frequency earthquakes. The events are displayed within 500 m above and below each inverted depth with reference to sea level. The low-frequency earthquakes, located beneath the caldera in the southeastern quadrant, are interpreted to be related with the existence of viscous magma linked to a cryptodome formation (Soosalu et al., 2006). The low-frequency events occur near the zones of low *S* wave velocity anomalies (Figures 13 and 15d2) supporting the hypothesis of Soosalu et al. (2006). The high-frequency earthquakes, interpreted as brittle failure of the volcanic edifice, are located in areas where we see high or average velocity anomalies. These earthquakes possibly related to fracturing due to thermal cracking (Soosalu & Einarsson, 1997) or crystallization processes (Scheiber-Enslin et al., 2011), are therefore expected to be around average to high *S* wave velocity anomalies. The cross sections of the *S* wave velocity field depicted in Figures 15a2–15d2 provide additional insight on the spatial distribution of the discussed anomalies. Vertical cross sections crossing the south area beneath the caldera show lower *S* wave velocities than elsewhere within the caldera outline (e.g., cross sections a2 and d2 crossing the south part beneath the caldera as opposed to b2 and c2 crossing the northern area).

High-velocity anomalies with a ring like structure, and following the shape and location of the caldera outline, contour the low-velocity anomaly (Figure 13 NE quadrant between 4- and 5-km depth). The strong high-velocity anomalies following the north and northeast quadrant, correlate well with lavas erupted at the surface (black arrows in Figure 12 and 13). We interpret these as solidified eruption-feeding dikes, possibly corresponding to the Brandsgil (115,000 to 130,000 years before present) and Jokulgil (65,000 to 115,000) series of erupted rhyolites (Ivarsson, 1992; Figure 15e). A feature catching the eye in the corresponding cross

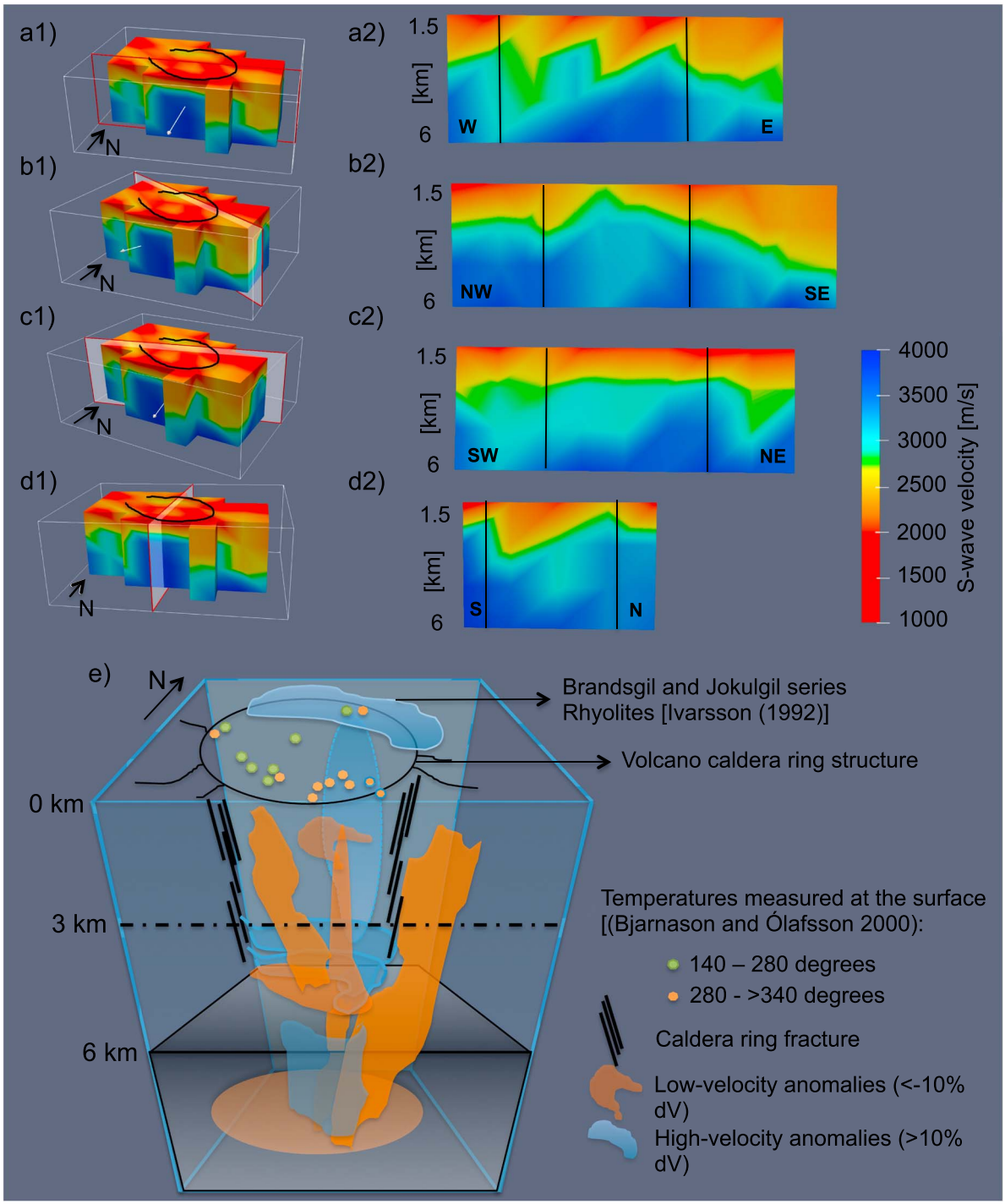

Figure 15. (a to d) Vertical cross sections of *S* wave velocities with corresponding locations (a1 to d1) and directions (a2 to d2). The black circle locates the volcano caldera which is projected to depth by the vertical black lines from a1 to d1. (e) Conceptual model of Torfajökull's volcano. The circle at 0-km depth is a conceptual representation of the volcano caldera with the remaining features identified in the legend figure (vertical exaggeration of approximately 4 times).

sections (Figure 15) is the abrupt change in velocity at the location of the caldera outline (vertical lines from a2 to d2) possible due to the caldera collapse structure. Approaching the caldera outline from the outside to inside, we observe an increase of the *S* wave velocity until it reaches the caldera outline location and then an immediate decrease. The change of speed occurs with a *S* wave velocity peak in the neighborhood of the caldera outline. This is the case for most of the cross sections we observe except for the cross section c2. This exception may be because of different reasons. In the NE part of the caldera we observe higher velocities

interpreted as old dike intrusions, therefore the high velocity anomalies might be overlapping the described caldera feature. In the west area the caldera, the described caldera feature might not be identified because at this area the caldera does not have surface manifestation. Note, that the vertical lines are projected vertically at depth. Therefore the (probably existing) dipping angle of the caldera fracturing at depth is not well represented here.

The overall *S* wave velocity field (Figures 15a–15d), reveals anisotropy, which is typical for volcanic environments and can be accentuated by the magma mixing style of Torfajökull's eruptions (Blake, 1984; McGarvie, 1984). We propose a conceptual model of Torfajökull's magmatic system based on the tomographic results of this manuscript (Figure 15e). The area where high-temperature geothermal activity is concentrated (> 140°C; Bjarnason & Ólafsson, 2000) is mostly located at the southeastern site within the volcano caldera and correlates well with dip in *S* wave velocities in the cross section d1-d2 of the same figure. At this stage we interpret Torfajokull's plumbing system up to 6-km depth as being composed of possible molten or partial molten cavities and channels (orange features in Figure 15e) relatively small when compared with Torfajokull's caldera size. We display the location the most prominent high-velocity anomaly in the northeastern site (blue ellipse) beneath the volcano caldera, interpreted to be the dike intrusion in origin of the Brandsgil and Jokulgil rhyolite eruptions.

These results indicate that if there is an established magma chamber within Torfajökull's caldera, it is likely to be deeper than analyzed depths. However, the shallowest part of it may also start at 4- to 5-km depth as indicated by the detected low-velocity anomalies. In case the low-velocity areas (velocity variations lower than −10%) are related to the presence of molten or partially molten rock at the estimated depths, three areas may be prone of eruption once the system is pressurized: the eastern and southwestern sites outside the caldera outskirts and the southeast area beneath the volcano caldera.

7. Conclusions

We applied surface wave tomography to Rayleigh waves estimated with ambient noise SI, to image Torfajökull's subsurface. We applied this methodology using only 100 days of ambient noise data but with an approach that relies on a strong quality selection of interstation traveltimes and reliable phase velocity estimation from retrieved surface waves. We removed frequencies for which the best fitting phase term of the virtual source does not come close to a physical source term. We successfully detect velocity variations between approximately 1.5- and 6-km depth, with a horizontal resolution of 4 km.

Northeast along the caldera outline, we identify high-velocity structures that might correspond to cold (rhyolitic) dikes. Outside the caldera, to the southwest and east, there are low-velocity anomalies that may indicate the presence of warm bodies. Even though we detect low-velocity anomalies inside the caldera deeper than 4-km depth, the low anomalies outside the volcano caldera are more prominent. As none of the identified features resembles a hot, established magma chamber beneath the caldera, we suggest that if a crustal magma chamber does exist beneath Torfajökull's caldera, it must be located below 6-km depth. The shallowest part of it may, however, start from 3.5-km depth onward as suggested by the detected low-velocity anomalies inside the volcano caldera. Our results suggest new opportunities for the application of ambient noise SI even to short acquisition time campaigns, especially in ocean-noise-prone areas like Iceland.

Acknowledgments
This study was supported by the Portuguese Foundation for Science and Technology (FCT-DFRH-SFRH/BD/61663/2009) and developed in the framework of FUTUREVOLC project (FUTUREVOLC has received funding from the European Union's Seventh Programme for research, technological development and demonstration under grant agreement 308377). The seismic data for this paper are archived at the IRIS data center. The final model and model uncertainty is included in digital form in the supporting information. The research of Elmer Ruigrok is supported by the Sustainability/GeoResources Programme of Utrecht University. The research of Deyan Draganov is supported by the Division for Earth and Life Sciences (ALW) with financial aid from the Netherlands Organization for Scientific Research (NWO) with VIDI grant 864.11.009. We would like to thank National Energy Authority of Iceland (Orkustofnun) and Iceland Geosurvey (ISOR) for financing the 2005 Torfajökull field campaign. We thank the Natural Environment Research Council for the loan of seismometers from SEIS-UK. The authors are grateful to Robert Nowack, Martha Savage, and the reviewers for their comments, which considerably improved the manuscript. Thanks are further given to P. Dheenathayalan for the interesting discussions on how to better display a magma chamber. Figure 1 of this publication has been produced with the aid of the freeware GMT (Wessel & Smith, 1991) and Figure 15 with Paraview (Ahrens et al., 2005).

References

Ahrens, J., Geveci, B., & Law, C. (2005). Paraview: An end-user tool for large data visualization. The visualization handbook, 717.

Aki, K. (1957). Space and time spectra of stationary stochastic waves, with special reference to microtremors. *Bulletin of the Earthquake Research Institute*, *35*, 415–456.

Aki, K. (1965). A note on the use of microseisms in determining the shallow structures of the Earth's crust. *Geophysics*, *30*(4), 665–666.

Båth, M. (1953). Comparison of microseisms in Greenland, Iceland, and Scandinavia. *Tellus*, *5*(2), 109–134.

Behr, Y., Townend, J., Bannister, S., & Savage, M. (2011). Crustal shear wave tomography of the Taupo Volcanic Zone, New Zealand, via ambient noise correlation between multiple three-component networks. *Geochemistry, Geophysics, Geosystems*, *12*, Q03015. https://doi.org/10.1029/2010GC003385

Bensen, G., Ritzwoller, M., Barmin, M., Levshin, A., Lin, F., Moschetti, M., & Yang, Y. (2007). Processing seismic ambient noise data to obtain reliable broad-band surface wave dispersion measurements. *Geophysical Journal International*, *169*(3), 1239–1260.

Bensen, G., Ritzwoller, M., & Shapiro, N. (2008). Broadband ambient noise surface wave tomography across the United States. *Journal of Geophysical Research*, *113*, B05306. https://doi.org/10.1029/2007JB005248

Bjarnason, J., & Ólafsson, M. (2000). Chemical composition of geothermal steam and hot water at Torfajökull. National Energy Authority of Iceland, Report OS-2000, 30, 91.

Blake, S. (1984). Magma mixing and hybridization processes at the alkalic, silicic, Torfajökull central volcano triggered by tholeiitic Veidivötn fissuring, south Iceland. *Journal of Volcanology and Geothermal Research*, *22*(1-2), 1–31.

Brandsdóttir, B., & Einarsson, P. (1992). Volcanic tremor and low-frequency earthquakes in Iceland. In *Volcanic seismology* (pp. 212–222). Berlin, Heidelberg: Springer.

Brenguier, F., Shapiro, N. M., Campillo, M., Nercessian, A., & Ferrazzini, V. (2007). 3-D surface wave tomography of the Piton de la Fournaise volcano using seismic noise correlations. *Geophysical research letters*, *34*, L02305. https://doi.org/10.1029/2006GL028586

Bromirski, P. D., & Duennebier, F. K. (2002). The near-coastal microseism spectrum: Spatial and temporal wave climate relationships. *Journal of Geophysical Research*, *107*(B8), ESE–5. https://doi.org/10.1029/2001JB000265

Claerbout, J. F. (1968). Synthesis of a layered medium from its acoustic transmission response. *Geophysics*, *33*(2), 264–269.

Draganov, D., Wapenaar, K., Mulder, W., Singer, J., & Verdel, A. (2007). Retrieval of reflections from seismic background-noise measurements. *Geophysical Research Letters*, *34*, L04305. https://doi.org/10.1029/2006GL028735

Einarsson, P. (1991). Earthquakes and present-day tectonism in Iceland. *Tectonophysics*, *189*(1), 261–279.

Einarsson, P., & Saemundsson, K. (1987). Earthquake epicenters 1982–1985 and volcanic systems in Iceland: Upptok Jardskjalfta 1982–1985 Og Eldstodvakerfi a Islandi. Menningarsjodur.

Gerstoft, P., & Tanimoto, T. (2007). A year of microseisms in Southern California. *Geophysical Research Letters*, *34*, L20304. https://doi.org/10.1029/2007GL031091

Golub, G. H., Heath, M., & Wahba, G. (1979). Generalized cross-validation as a method for choosing a good ridge parameter. *Technometrics*, *21*(2), 215–223.

Gunnarsson, B., Marsh, B., & Taylor, H. Jr (1998). Generation of Icelandic rhyolites: Silicic lavas from the Torfajökull central volcano. *Journal of Volcanology and Geothermal Research*, *83*(1), 1–45.

Haubrich, R., Munk, W., & Snodgrass, F. (1963). Comparative spectra of microseisms and swell. *Bulletin of the Seismological Society of America*, *53*(1), 27–37.

Ivarsson, G. (1992). Geology and petrochemistry of the Torfajökull central volcano in central south Iceland, in association with the Icelandic hot spot and rift zones. UMI Dissertation Services.

Jaxybulatov, K., Shapiro, N., Koulakov, I., Mordret, A., Landès, M., & Sens-Schönfelder, C. (2014). A large magmatic sill complex beneath the Toba caldera. *science*, *346*(6209), 617–619.

Kang, T. S., & Shin, J. S. (2006). Surface-wave tomography from ambient seismic noise of accelerograph networks in southern Korea. *Geophysical Research Letters*, *33*, L17303. https://doi.org/10.1029/2006GL027044

Kao, H., Behr, Y., Currie, C. A., Hyndman, R., Townend, J., Lin, F. C., & He, J. (2013). Ambient seismic noise tomography of Canada and adjacent regions: Part I. Crustal structures. *Journal of Geophysical Research: Solid Earth*, *118*, 5865–5887. https://doi.org/10.1002/2013JB010535

Kusche, J., & Klees, R. (2002). Regularization of gravity field estimation from satellite gravity gradients. *Journal of Geodesy*, *76*(6-7), 359–368.

Lacoss, R., Kelly, E., & Toksoz, M. (1969). Estimation of seismic noise structure using arrays. *Geophysics*, *34*(1), 21–36.

Larose, E., Khan, A., Nakamura, Y., & Campillo, M. (2005). Lunar subsurface investigated from correlation of seismic noise. *Geophysical Research Letters*, *32*, L16201. https://doi.org/10.1029/2005GL023518

Lévêque, J. J., Rivera, L., & Wittlinger, G. (1993). On the use of the checker-board test to assess the resolution of tomographic inversions. *Geophysical Journal International*, *115*(1), 313–318.

Lin, F. C., Moschetti, M. P., & Ritzwoller, M. H. (2008). Surface wave tomography of the western United States from ambient seismic noise: Rayleigh and Love wave phase velocity maps. *Geophysical Journal International*, *173*(1), 281–298.

Lippitsch, R., White, R., & Soosalu, H. (2005). Precise hypocentre relocation of microearthquakes in a high-temperature geothermal field: The Torfajökull central volcano, Iceland. *Geophysical Journal International*, *160*(1), 371–388.

Luzón, F., Almendros, J., & García-Jerez, A. (2011). Shallow structure of Deception Island, Antarctica, from correlations of ambient seismic noise on a set of dense seismic arrays. *Geophysical Journal International*, *185*(2), 737–748.

Masterlark, T., Haney, M., Dickinson, H., Fournier, T., & Searcy, C. (2010). Rheologic and structural controls on the deformation of Okmok volcano, Alaska: FEMs, InSAR, and ambient noise tomography. *Journal of Geophysical Research*, *115*, B02409. https://doi.org/10.1029/2009JB006324

McGarvie, D. W. (1984). Torfajokull: A volcano dominated by magma mixing. *Geology*, *12*(11), 685–688.

Mordret, A., Rivet, D., Landès, M., & Shapiro, N. M. (2014). 3-D shear-velocity anisotropic model of Piton de la Fournaise volcano (La Réunion Island) from ambient seismic noise. *Journal of Geophysical Research: Solid Earth*, *120*, 406–427. https://doi.org/10.1002/2014JB011654

Nagaoka, Y., Nishida, K., Aoki, Y., Takeo, M., & Ohminato, T. (2012). Seismic imaging of magma chamber beneath an active volcano. *Earth and Planetary Science Letters*, *333*, 1–8.

Park, C. B., Miller, R. D., & Xia, J. (1998). Imaging dispersion curves of surface waves on multi-channel record. SEG Expanded Abstracts Seg expanded abstracts vol. 17, pp. 1377–1380.

Park, C. B., Miller, R. D., & Xia, J. (1999). Multichannel analysis of surface waves. *Geophysics*, *64*(3), 800–808.

Peterson, J. (1993). Observations and modeling of seismic background noise. US Geological Survey.

Rost, S., & Thomas, C. (2002). Array seismology: Methods and applications. *Reviews of geophysics*, *40*(3), 1008. https://doi.org/10.1029/2000RG000100

Roux, P., Sabra, K. G., Gerstoft, P., Kuperman, W., & Fehler, M. C. (2005). *P*-waves from cross-correlation of seismic noise. *Geophysical Research Letters*, *32*, L19303. https://doi.org/10.1029/2005GL023803

Ruigrok, E., Campman, X., & Wapenaar, K. (2011). Extraction of *P*-wave reflections from microseisms. *Comptes Rendus Geoscience*, *343*(8), 512–525.

Ruigrok, E., Gibbons, S., & Wapenaar, K. (2017). Cross-correlation beamforming. *Journal of Seismology*, *21*(3), 495–508.

Sabra, K. G., Gerstoft, P., Roux, P., Kuperman, W., & Fehler, M. C. (2005a). Extracting time-domain Green's function estimates from ambient seismic noise. *Geophysical Research Letters*, *32*, L03310. https://doi.org/10.1029/2004GL021862

Sabra, K. G., Gerstoft, P., Roux, P., Kuperman, W., & Fehler, M. C. (2005b). Surface wave tomography from microseisms in Southern California. *Geophysical Research Letters*, *32*, L14311. https://doi.org/10.1029/2005GL023155

Sambridge, M. (1999a). Geophysical inversion with a neighbourhood algorithm—II. Appraising the ensemble. *Geophysical Journal International*, *138*(3), 727–746.

Sambridge, M. (1999b). Geophysical inversion with a neighbourhood algorithm—I. Searching a parameter space. *Geophysical Journal International*, *138*(2), 479–494.

Scheiber-Enslin, S. E., LaFemina, P. C., Sturkell, E., Hooper, A. J., & Webb, S. J. (2011). Geodetic investigation of plate spreading along a propagating ridge: The Eastern Volcanic Zone, Iceland. *Geophysical Journal International*, *187*(3), 1175–1194.

Sella, G. F., Dixon, T. H., & Mao, A. (2002). REVEL: A model for recent plate velocities from space geodesy. *Journal of Geophysical Research*, *107*(B4), 2081. https://doi.org/10.1029/2000JB000033

Shapiro, N. M., & Campillo, M. (2004). Emergence of broadband Rayleigh waves from correlations of the ambient seismic noise. *Geophysical Research Letters*, *31*, L07614. https://doi.org/10.1029/2004GL019491

Shapiro, N. M., Campillo, M., Stehly, L., & Ritzwoller, M. H. (2005). High-resolution surface-wave tomography from ambient seismic noise. *Science*, *307*(5715), 1615–1618.

Shapiro, N. M., Ritzwoller, M. H., Molnar, P., & Levin, V. (2004). Thinning and flow of Tibetan crust constrained by seismic anisotropy. *Science*, *305*(5681), 233–236.

Snieder, R. (2004). Extracting the Green's function from the correlation of coda waves: A derivation based on stationary phase. *Physical Review E*, *69*(4), 046610.

Soosalu, H., & Einarsson, P. (1997). Seismicity around the Hekla and Torfajökull volcanoes, Iceland, during a volcanically quiet period, 1991–1995. *Bulletin of volcanology*, *59*(1), 36–48.

Soosalu, H., & Einarsson, P. (2004). Seismic constraints on magma chambers at Hekla and Torfajökull volcanoes, Iceland. *Bulletin of Volcanology*, *66*(3), 276–286.

Soosalu, H., Lippitsch, R., & Einarsson, P. (2006). Low-frequency earthquakes at the Torfajökull volcano, south Iceland. *Journal of volcanology and geothermal research*, *153*(3), 187–199.

Stankiewicz, J., Ryberg, T., Haberland, C., & Natawidjaja, D. (2010). Lake Toba volcano magma chamber imaged by ambient seismic noise tomography. *Geophysical Research Letters*, *37*, L17306. https://doi.org/10.1029/2010GL044211

Stutzmann, E., Ardhuin, F., Schimmel, M., Mangeney, A., & Patau, G. (2012). Modelling long-term seismic noise in various environments. *Geophysical Journal International*, *191*(2), 707–722.

Tanimoto, T., & Prindle, K. (2007). Surface wave analysis with beamforming. *Earth, Planets, and Space*, *59*(5), 453–458.

Tikhonov, A. (1963). On the solution of ill-posed problems and the method of regularization. *Dokl. Akad. Nauk SSSR*, *151*(3), 501–504.

Tsai, V. C., & Moschetti, M. P. (2010). An explicit relationship between time-domain noise correlation and spatial autocorrelation (SPAC) results. *Geophysical Journal International*, *182*(1), 454–460.

Tuffen, H. (2007). Models of ice melting and edifice growth at the onset of subglacial basaltic eruptions. *Journal of Geophysical Research*, *112*, B03203. https://doi.org/10.1029/2006JB004523

Villagómez, D. R., Toomey, D. R., Hooft, E. E., & Solomon, S. C. (2011). Crustal structure beneath the Galápagos Archipelago from ambient noise tomography and its implications for plume-lithosphere interactions. *Journal of Geophysical Research*, *116*, B04310. https://doi.org/10.1029/2010JB007764

Villasenor, A., Yang, Y., Ritzwoller, M. H., & Gallart, J. (2007). Ambient noise surface wave tomography of the Iberian Peninsula: Implications for shallow seismic structure. *Geophysical Research Letters*, *34*, L11304. https://doi.org/10.1029/2007GL030164

Wapenaar, K. (2004). Retrieving the elastodynamic Green's function of an arbitrary inhomogeneous medium by cross correlation. *Physical review letters*, *93*(25), 254301.

Wapenaar, K., & Fokkema, J. (2006). Green's function representations for seismic interferometry. *Geophysics*, *71*(4), SI33–SI46.

Wathelet, M. (2008). An improved neighborhood algorithm: Parameter conditions and dynamic scaling. *Geophysical Research Letters*, *35*, L09301. https://doi.org/10.1029/2008GL033256

Wathelet, M., Jongmans, D., & Ohrnberger, M. (2004). Surface-wave inversion using a direct search algorithm and its application to ambient vibration measurements. *Near Surface Geophysics*, *2*(4), 211–221.

Weaver, R. L., & Lobkis, O. I. (2004). Diffuse fields in open systems and the emergence of the Green's function (L). *The Journal of the Acoustical Society of America*, *116*(5), 2731–2734.

Wessel, P., & Smith, W. H. (1991). Free software helps map and display data. *Eos, Transactions American Geophysical Union*, *72*(441), 445–446.

Yang, Y., Ritzwoller, M. H., Levshin, A. L., & Shapiro, N. M. (2007). Ambient noise Rayleigh wave tomography across Europe. *Geophysical Journal International*, *168*(1), 259–274.

Yao, H., van Der Hilst, R. D., & Maarten, V. (2006). Surface-wave array tomography in SE Tibet from ambient seismic noise and two-station analysis—I. Phase velocity maps. *Geophysical Journal International*, *166*(2), 732–744.

Yokoi, T., & Margaryan, S. (2008). Consistency of the spatial autocorrelation method with seismic interferometry and its consequence. *Geophysical Prospecting*, *56*(3), 435–451.